Synthesis and Characterization of Lithium-Ion Based Diatom Batteries

By

Nicholas Aigner Wright

Thesis

Submitted to the Faculty of the

Graduate School of Vanderbilt University

in partial fulfillment of the requirements

for the degree of

MASTER OF SCIENCE

in

Chemistry

May, 2016

Nashville, Tennessee

Approved:

David Wilson Wright, Ph.D.

David Edward Cliffel, Ph.D.

TABLE OF CONTENTS

Page

LIST OF FIGURES

ABSTRACT

New and innovative materials are needed to develop more effective batteries. Nanoscale materials such as graphite have unique properties only seen in the nano-regime that allow them to be used in the production of lithium-ion batteries. For example, because of its ability to conduct electricity, nano-scale graphite has been used in the anode of lithium-ion batteries, which has revolutionized the long-term use of medical devices, such as pacemakers and defibrillators. Interestingly, the graphite anode has a relatively low specific capacity per gram of ~372 mAh g^{-1}, which limits the rate of charge available to these devices. The specific capacity of silicon, however, is ~11 times greater than that of graphite at ~4200 mAh g^{-1}, which makes it a better choice as an anode material. Silicon is not presently used because of its fragility during the lithiation process. In this work, we demonstrate a robust nanoscale material synthesis inspired by the biomineralization process that the ocean-dwelling unicellular phytoplankton, diatoms, that they use to form their porous silicon structure. By maintaining the porous structure of diatoms from the conversion of silica to silicon, using a magnesiothermic reduction process, their structure can be used to enhance silicon's strength during the lithiation process allowing the use of silicon's higher specific capacity. This approach has the potential to implement silicon as an anode for lithium-ion batteries to enhance the longevity of present day applications.

Chapter 1

GENERAL INTRODUCTION

As the world continues to grow, the energy demand continues to increase with the rising population. Due to the rapid increase in the use of portable computers, mobile phones, video cameras, electric vehicles, and other portable technologies, there is a mounting demand for larger capacity, smaller size, lighter weight, and lower priced rechargeable batteries to power these technologies. The dominant rechargeable battery chemistry for consumer electronics (e.g., smart phones and notebook computers) and medical devices (e.g., implantable cardioverter defibrillators (ICDs) and pacemakers) is the lithium-ion battery (LIB). This technology is poised to become commonplace for industrial, transportation, and power-storage applications. Lithium-ion battery chemistry is different from previously popular rechargeable battery chemistries e.g., nickel metal hydride (NiMH), nickel cadmium (NiCd), and lead acid, in a number of ways. LIB's provide a higher energy density, a higher cell voltage, require no routine maintenance, there is no memory effect associated, possess a higher cycle life, lightweight, and they are compact.[2] From a technological standpoint, because of high energy density, LIB technology has enabled entire families of portable devices, such as laptops and smart phones to thrive in today's society. The current anode used in lithium-ion batteries possesses graphene due to its ability to intercalate lithium-ions in and out of the graphene layers efficiently.

The increasing demand for better, longer lasting, energy storage devices is continuously growing and the field is ever expanding with new technological advancements and consumer interests. As a result, energy supplies are ever tightening and with every new innovation that

deals with heavy metals, toxic substrates, or energy intensive fabrication methods, there are environmental concerns that must be addressed. This slows down the process of constructing better energy supplies and storage devices, thus requiring mankind to think innovatively and to develop new energy supplies, storage, and more efficient electronics. By looking to nature for an answer to this current problem, we find that numerous organisms can produce ornately detailed inorganic structures with features on length scales of 50 nm to several centimeters. These structures are created under the organism's unique pathways to create hierarchical structures that are utilized by the organism for shelter, protection, or other functions that the organism needs in order to survive and live. Looking directly at biogenic and bio-based hierarchical structures brought about by the nano-scale biomineralization process of phytoplankton, specifically diatoms, this could be a new direction for energy and energy storage materials.

Diatoms are unicellular photosynthetic algae that belong to the class Bacillariophyceae.[3] Within this class there are over 100,000 extant diatom species known, each endowed with their own individual genetically determined, unique and ornate patterns of silica that make up the cytoskeleton structure. Almost all diatoms utilize the process of biomineralization, the study of the formation, structure, and properties of inorganic solids deposited in biological systems.[4] A more precise definition in the case of diatoms is the process of biosilicification, where an organism uptakes soluble silicon precursors from the environment and precipitates the silicon into amorphous silicon oxides. While diatoms are not the only organisms to utilize silicon to build biological structures, they are the largest contributor to biosilicification on earth.[5,6] Most diatoms perform this process and make uniquely shaped silica nanoparticle based micro-shells or "glass houses" called frustules. This unique structure processes hierarchical micro- and nano-scale features made by a bottom-up approach at ambient temperatures and pressures. The

available morphologies the extant species are capable of making are, but not limited to, hollow cylinders, disks, interlocking 'barbs', high aspect ratio needles, trigonal, triangular, elliptical, and star structures. The structural features of the diatom's frustule are periodic, two–dimensional pore arrays that perforate the frustule. These arrays have lattice constants at the submicron to nanoscale and the pores themselves are often embedded with nanoscale features. A review on the unique structures and diversity of the diatom genera can be found in The Diatoms: Biology & Morphology of the Genera.[3,7] It has been known for over a century that diatoms are comprised of silicon.[8] However it was not proven until 1955 that diatoms incorporate silicon into its structure from their external environment.[9] The uptake of silicon precursors seen in diatoms was later proven to be carrier-mediated by silicon transport proteins (SiTs) in the cell wall of the diatom.[10,11] The SiTs transports silicic acid, $Si(OH)_4$, across the cell wall from the cell culture medium into the cytoplasm.

Preceding cell separation in the cell division process, soluble silicon in the cytoplasm is transported by molecular diffusion or by silicic acid transporters to the silicon deposition vesicle.[12] The silicon deposition vesicle (SDV) is a specialized cell compartment located along the central axis of a diatom, midway between the epivalve and hypovalve, which are the two Petri dish shaped halves of the cell wall. A membrane called the silicalemma binds the SDV, and it is within this specialized compartment where soluble silicon is polymerized to form silica.[13] The SDV contains specialized proteins called silaffins as well as long chain poly-amines (LCPAs), which catalyze a hydrolysis reaction that links silicic acid monomers together to form solid silica (SiO_2) by the creation of siloxane (Si-O-Si) bonds.[14-16] The silicon oxide is formed into nanospheres embedded with the silaffin proteins and LCPAs by a phase separation reaction.

The nano-sized amorphous silica building blocks are used to construct the patterned micro and nano-structures that become new diatom frustules.[14,16-21]

The frustule structure is passed indefinitely from parent to progeny through genetic information. Barring substrate limitations, diatoms grow exponentially with time, making the fabrication of the hierarchical structures both highly reproducible and scalable. Diatom silica has some use as a chemical sensor, but in its native form diatom silica cannot be used for energy production or optoelectronic device fabrication due to the inertness of amorphous silica. The silica therefore must be modified in order to become useful.[22]

Chapter 2

SYNTHESIS AND CHARACTERIZATION OF DIATOMACEOUS EARTH TO ELEMENTAL SILICON

Introduction

The increasing demand for high-energy, high-power density, and high rate capability lithium ion batteries (LIBs) has continued to grow and expand with new technological advances and consumer demand. Currently, carbon-based materials are the most common anode in commercial LIBs, but their specific capacity is relatively low (370 mA h g^{-1}) and their charge/discharge rate is low as well.[23] Silicon (Si) is a promising alternative over carbon, with a high theoretical capacity of 4212 mA h g^{-1} ($Li_{4.4}Si$).[24] Silicon-based electrodes, however, undergo large volume expansion during cycling of approximately 400%. This can cause pulverization and deterioration of the anode upon compression to its original crystal lattice, which creates a loss of electrical conductivity leading to poor cycling performance.

To overcome this problem, various silicon nanostructures have been fabricated such as nanoparticles, nanowires, and other nanoshapes. The Si nanostructures show relatively excellent electrochemical properties, but the fabrication of nanostructured Si commonly requires complicated routes with toxic precursors or high-cost techniques.[25-27] An alternative and green approach to these fabrication methods is using readily available sources of silica found in diatomaceous earth. These silica nanostructures of the diatom's frustules are created by the organism using biomineralization, self-assembly by polycondensation of silicic acid, $Si(OH)_4$.

This low-cost approach for nanostructured silicon by using diatomaceous earth is a great alternative to the high-cost, high-processing methods that are currently being implemented.

Experimental

General Considerations and Materials

All syntheses were conducted under rigorous exclusion of air and moisture using Schlenk-line or glove box techniques under argon or nitrogen as needed based on the nature of the experiment. Stainless steel (440 grade) ball bearings (4 mm) and BMT-20-S tubes were purchased from IKA. The ball bearings were thoroughly cleaned with hexanes and acetone prior to use. Disperser milling was performed with an Ultra-Turrax Tube Drive borrowed from the Hanusa Laboratory. Powdered magnesium (-325 mesh) was purchased from Alfa Aesar, kept in an inert (argon) atmosphere, and used as received. Brass Swagelok tube fitting, Union, 1 inch tube outer diameter (OD) (B-1610-6) and (2) 316 stainless steel (SS) plug for 1 inch Swagelok tube fitting (SS-1610-P) were used to construct reduction chamber #1. SS Swagelok® tube fitting, Union, 1 inch tube OD (SS-1610-6) and 2-brass plug for 1 inch Swagelok tube fitting (B-1610-P) were used to construct reduction chamber #2. All stainless steel and brass parts were purchased from Swagelok. The tube furnace used for reduction was a Lindberg Blue programmable tube furnace 1.5 in diameter. Powder x-ray diffraction (XRD) used for this experiment was a Scintag X_1 θ/θ automated powder diffractometer with a Cu target, a Peltier-cooled solid-state detector, and a zero-background, Si (510) sample support or amorphous plastic support.

A device was constructed in this project using the above-mentioned Swagelok® materials to construct an airtight chamber for reducing silica to silicon. The magnesiothermic reduction

chamber (MTRC) is assembled using dissimilar metals and Permatex ® Anti-Seize Lubricant (Rated for temperatures of up to 870˚C). Dissimilar metals are employed in constructing this chamber for the union versus the plugs being used, *e.g.* brass union with steel plugs or a steel union with brass plugs, so that the plugs and the union do not fuse together during the heating process.

Synthesis (Reduction) of Elemental Silicon (Diatomaceous Earth)

Diatomaceous earth was purchased from Sigma Aldrich and the frustules were cleaned by first soaking the material in 10% (v/v) hydrochloric acid (HCl) solution for 8 hours at 80°C to remove any metal impurities in or associated to the frustule by forming metal-chlorides. After washing with 10% HCl, the solid material is recovered by centrifugation at 3,000 rpms for 5 minutes. This was performed three times and the washed material was then transferred onto a quartz combustion boat and spread as flat as possible for maximum surface area coverage to make sure all the material was exposed evenly in the tube furnace. The boat was then placed into a tube furnace and set to 800°C at a ramp rate of 5°C per minute for 3 hours to remove any organic material from the frustule.

Approach #1

Uses an air-sensitive approach to remove oxygen from the system. Frustules, cleaned of metal impurities and organic matter, were placed into a magnesiothermic reduction chamber with magnesium turnings or powder found in the chemical repository. These components were placed into a glove bag and the system was purged with argon (Ar). Once an Ar system was achieved, 500 mg of diatomaceous earth and 500 mg of magnesium where placed into the magnesiothermic reduction chamber, then the chamber was assembled.

Approach #2

Uses an air-sensitive approach with milling to solve the problems from Approach #1. Once the frustules were cleaned of metal impurities and organic matter, 0.15 grams of the frustules (silica) were placed into a disperser tube with 15 stainless steel ball bearings. This disperser tube was pumped into an argon (Ar) glove box and evacuated. A 3.5 mole ratio of powdered magnesium to 1 mole of silica was combined into the tube. The tube was then closed shut and sealed with electrical tape before being pumped out of the glove box. The tube was placed on an Ultra-Turrax Tube Drive and milling was performed for 12 minutes. The disperser tube was placed into a glove bag and the bag was evacuated with argon. Once 10 minutes had passed to ensure an argon environment was achieved, the milled material was transferred into the magnesiothermic reduction chamber.

Approach #3

Employs a different method than the last 2 approaches, optimizing the preparation of the diatoms and optimizing Approach #2. Knowing that diatomaceous earth is a compilation of many different diatom species, a filtration approach can be utilized. With this large collection of diatoms, the dimensions of diatoms can range from 2 μm to 500 μm.[3,28] With such a range of dimensions a Millipore® filter, at a 0.2 μm pore size, is employed. This filter is used to remove the diatoms from the HCL solution and wash them with DI water. The filtrate forms a cake and is dissolved with a small amount of ethanol to evenly distribute the diatomaceous earth on the combustion weigh boat. The weigh boat is then placed in a 2-stage tube furnace. The first stage is set for 10 minutes at 90C at a ramp rate of 2.5C per minute to ensure that the ethanol is removed slowly so that the diatomaceous earth is disturbed at a minimal amount. The second

stage is then for 30 minutes at 700°C at a ramp rate of 5°C per minute. The material was then placed into a disperser tube with 15 ball bearings and placed under an Ar environment. A 3.5 mole ratio of powdered magnesium to 1 mole of silica was combined into the tube. The tube was then closed shut and sealed with electrical tape before being pumped out of the glove box. The tube was placed on an Ultra-Turrax Tube Drive and milling was performed for 12 minutes. The disperser tube was placed into a glove bag and the bag was evacuated with argon. Once 10 minutes had passed to ensure an argon environment was achieved, the milled material was transferred into the magnesiothermic reduction chamber.

Post Reaction and Recovery

After completing each approach, the MTRC was assembled and the chamber was placed onto a hand-made aluminum foil boat to aid in the preservation of the quartz tubing from scratching and forming cracks that could be made from the MTRC, and then transferred to the tube furnace. The temperature was set to 500˚C for 3 hours at a ramp rate of 5˚C per minute. The vessel was then allowed to cool over night after heating.

The vessel was loosened using a bench top vice and then brought into a glove bag. The contents of the vessel and a stir bar were transferred into the three-neck round bottom flask and sealed with the stoppers. The flask was moved from the glove bag and setup above a stir plate. Outlet and inlet needles are applied to the outside necks of the three-neck round bottom flask. A slow steady stream of nitrogen is allowed to fill the round bottom for a period of 5 minutes. After this time the addition of 1 M hydrochloric acid (HCl) solution was slowly injected into the closed round bottom by needle and syringe. An amount of HCl solution is added until violent bubbling has quenched the following reactions:

$$MgO_{(s)} + 2HCl_{(aq)} \rightarrow MgCl_{2(aq)} + H_2O_{(l)}$$

$$Mg_{(s)} + 2HCl_{(aq)} \rightarrow MgCl_{2(aq)} + H_{2(g)}$$

This cleanup step was allowed to stir overnight (about 16 hours). A color change from a clear transparent solution to a black opaque solution was observed after stirring. The precipitant is collected by centrifugation at 3,000 RPM for 5 minutes, washing 3 times in total, 1 with water and 2 washings with 95% ethanol, respectively. The collected material is then etched with 37% hydrofluoric acid (HF) for 1 hour, then centrifuged and etched again for 1 hour. The material is then allowed to dry in a vacuum oven overnight.

Graphene (Graphite) Coating

The graphene (graphite) coating that was adhered to the Si diatoms was performed in a 3-zone Lindberg Blue furnace with a 4" quartz tube. These Si diatom samples were loaded onto a custom-fabricated sample holder and placed in the center zone of the tube furnace. The sample was then placed under vacuum until 2–5 mTorr was reached. 1 SLM (standard liter per minute) of Ar and 200 SCCM (standard cubic centimeter per minute) of H_2 was utilized to maintain atmospheric pressure in the quartz tube while the furnace temperature was heated to 650°C. Once the furnace reached temperature, 10 SCCM of C_2H_2 (acetylene) was added to the gas flow and the temperature was increased to 750°C and held for 10 minutes at temperature, then increased another 100°C to 850°C and held for an additional 10 minutes. The C_2H_2 was turned off after the last 10 minute period and the newly carbon-coated Si diatoms were held in an Ar and H_2 atmosphere until the sample reached ~50°C when it was able to be touched by hand and removed from the furnace. The samples were stored in a N_2 glove box until devices were

fabricated from these materials. Analysis of the materials before and after coating was performed with a Zeiss Merlin SEM and a Renishaw inVia MicroRaman system.[29]

Battery Assembly

The anode was prepared by mixing the active material, carbon-coated silicon diatoms, with 20 wt.% carbon black and polyvinylidene fluoride (PVDF) binder in N-methyl-2-pyrrolidone (NMP) solvent to form a homogenous slurry. This slurry is spread onto a stainless steel disc, which serves as the current collector. The typical active mass loading of the electrodes was 2-3 mg cm^{-2}. Electrochemical characterizations were carried out using CR 2032 coin-type cells. CR 2032 coin-type cells were assembled in an argon-filled (O_2 and H_2O levels less than 1 ppm) MBRAUN glove box as seen in Figure 1. A Celgard® 2500 (25 μm thickness) monolayer porous polypropylene (PP) separator is placed atop the lithium foil counter electrode containing liquid electrolyte, then the carbon-coated Si diatom anode is placed on top followed by a wave spring and the cap. The electrolyte used was 1 molar LiPF6 in a 50:50 (w/w) mixture of ethylene carbonate (EC) and diethyl carbonate.

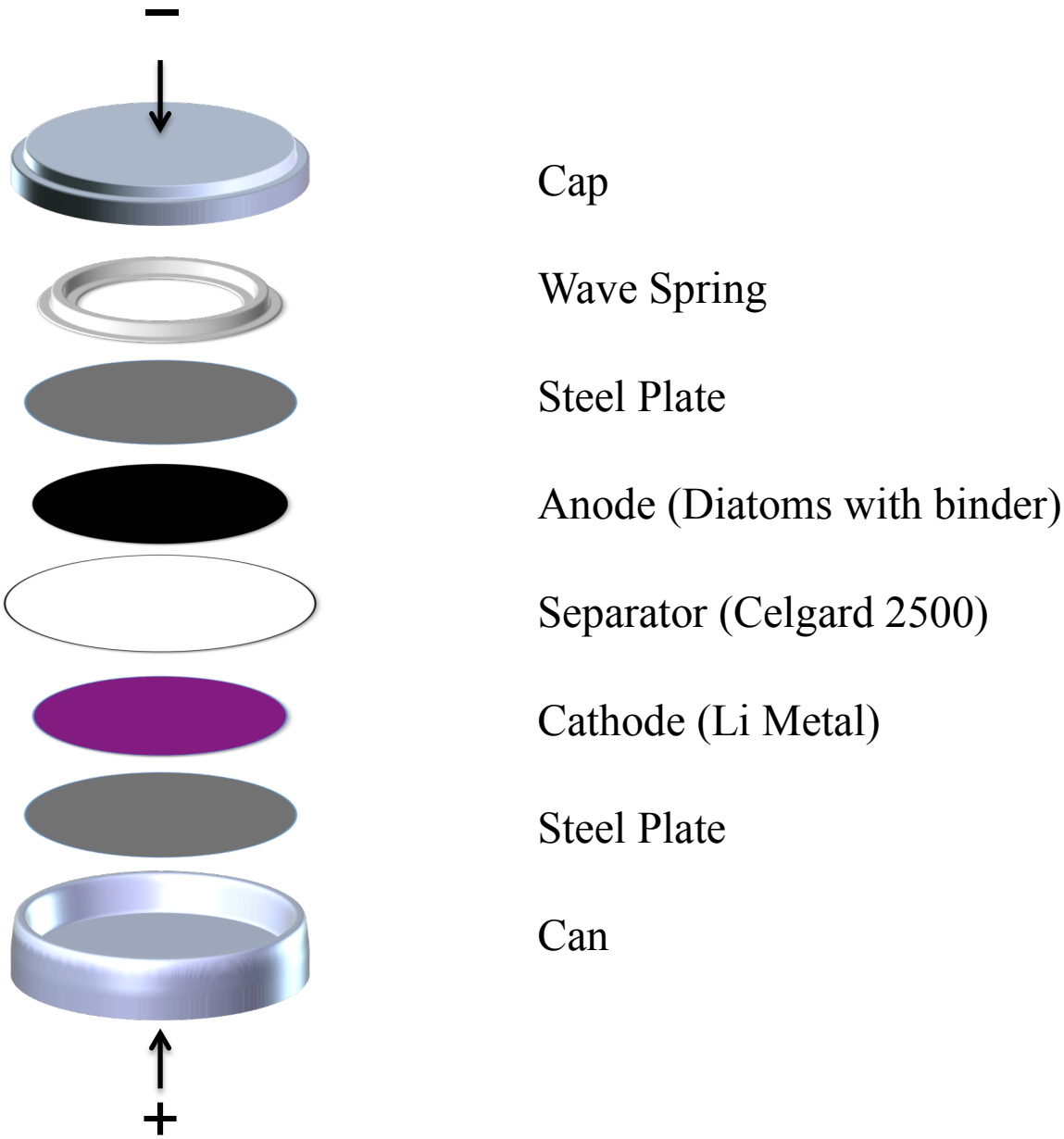

Figure 1: A 2032 coin cell diagram displaying how the Li coin cell is assembled with the incorporation of the Si diatoms.

Electrochemical Measurements

The coin cells used for the study were galvanostatically charged and discharged within a range of 0.02 – 2.0 V at a constant current density of 100 mA g^{-1}. The electrochemical measurements were taken on Metrohm Autolab multichannel testing system.

Results and Discussion

Looking at the result of each approach individually, Approach #1 yielded no silicon product. Varying the amounts of magnesium turnings used in the reaction yielded no silica converted to silicon. Similarly magnesium powder was used from the repository that had previously been opened to air. This yielded no reaction when used as well. The magnesium powder had most likely oxidized over time, leading to the inactivity observed in the reaction due to the inert reagent used.

Approaches #2 and #3 did yield the sought after product, converting silica to silicon while preserving the dynamic structure. The reaction that occurs inside the MTRC is a single-replacement reaction or a solid-state redox reaction between the magnesium (Mg) and the silicon dioxide (SiO_2).

$$SiO_{2(s)} + 2Mg_{(g)} \rightarrow Si_{(s)} + 2MgO_{(s)}$$

The solid magnesium in this reaction is the reducing agent and acts as a scavenger, sequestering the oxygen atoms from diatom frustules. Although the silica frustules found are amorphous silica, XRD data, seen in Figure 3 and Figure 4, has shown that the heat treatment at 700°C – 850°C can force the amphoricity of the silica frustule to an ordered quartz structure. The

exact polymorph of the quartz is hard to pinpoint as the transition from amorphous silica to quartz at these temperatures may have formed beta-quartz, then cooled to alpha-quartz. In this transition it is possible that the original beta-quartz shape is preserved, but is decreased in symmetry and the addition of trigonal crystal faces can occur. It is also possible that the beta quartz transforms into alpha quartz without losing symmetry, and therefore does not add the trigonal faces. These crystals are shaped as bipyrimidal hexagons and can be referred to as alpha-quartz paramorphs of beta-quartz.[30-32]

Assuming that a hexagonal crystal structure is present in the diatom frustules after the heat treatment, a comparison of this structure and the hexagonal close-pack crystal structure of magnesium can be considered. With these roughly similar crystal structures, solid-state diffusion may have taken during the heating process. The relative contribution of the different types of diffusion in oxides and other inorganic compounds are functions of the temperature, partial pressures or activities of the constituents of the compounds, the microstructure, grain size, and porosity, as well as many other factors that may contribute. The exact contributing factors for the solid-state diffusion in this reaction are not known, but by using the MTRC and the known reaction conditions described in the above approaches, it can be inferred that the elevated temperature conditions and the increased pressure conditions this experiment was held under, aided in the solid-state diffusion.

In addition to the experimental factors for this reaction, mechanochemical techniques where used in this reaction process. When the diatoms and the powdered magnesium where milled together for a 12 minute period, the milling process may have allowed for point defects to occur on the surface of the crystalline diatom frustule. This would have shifted the crystal lattice planes just slightly from its original structure. The shift then would have allowed interstitial sites

and vacancies found in quartz along with point defects to form and would allowed magnesium to interact with the oxygen in found in quartz.

Looking more closely at the reaction conditions used, ratios of magnesium to silica were tried and a 3:1 molar ratio of magnesium to silica shows an almost complete conversion of silica to silicon at 500°C. Using the ideal gas law and using the equation modification for moles as n = m/M (where m is equal to the grams of material and M is equal to the molar mass of the material), the estimated pressure, during the 3-hour reaction period, was calculated based on the dimensions of the MTRC, the volume capacity of the MTRC, the known amounts of the silica and magnesium, and the final temperature. The equation and experiment values for the calculated pressure can be found in Appendix A. The calculated pressure inside the MTRC was approximately 127 atm.

The Gibb's Free Energy for spontaneous reaction of magnesium oxide from oxygen and silica, respectively, are as follows:

$$2Mg_{(s)} + O_{2(g)} \rightarrow 2MgO_{(s)} \qquad \Delta G = -569 \text{ kJ/mol}$$

$$2Mg_{(s)} + SiO_{2(s)} \rightarrow 2MgO_{(s)} + Si_{(s)} \qquad \Delta G = -130 \text{ kJ/mol}$$

The MTRC is held under an argon environment to prevent advantageous oxygen from reacting with the magnesium. Due to the argon environment, the Gibb's Free Energy for magnesium would react preferentially with the silica. Any exposed oxygen due to point defects, vacancies, and/or interstitial sites will be converted to magnesium oxide from the silica as a result. Having a

high ratio amount of magnesium to silica in the MTRC helps to further drive the reaction as the magnesium reduces the silica.

Characterization of the silicon before it was incorporated it into the battery was performed using Raman on a Renishaw inVia system using a 532nm laser. After HF etching of the silicon diatoms, a Raman spectrum was taken to check the crystallinity of the silicon and to make sure the HF etching is removing any silica that may have formed from the HCl wash step. Figure 2 shows the Raman spectrum of the HF etched silicon diatoms. The accepted Raman signature of elemental silicon is 521 ± 1 cm^{-1}, which is seen in the Raman spectra.[33]

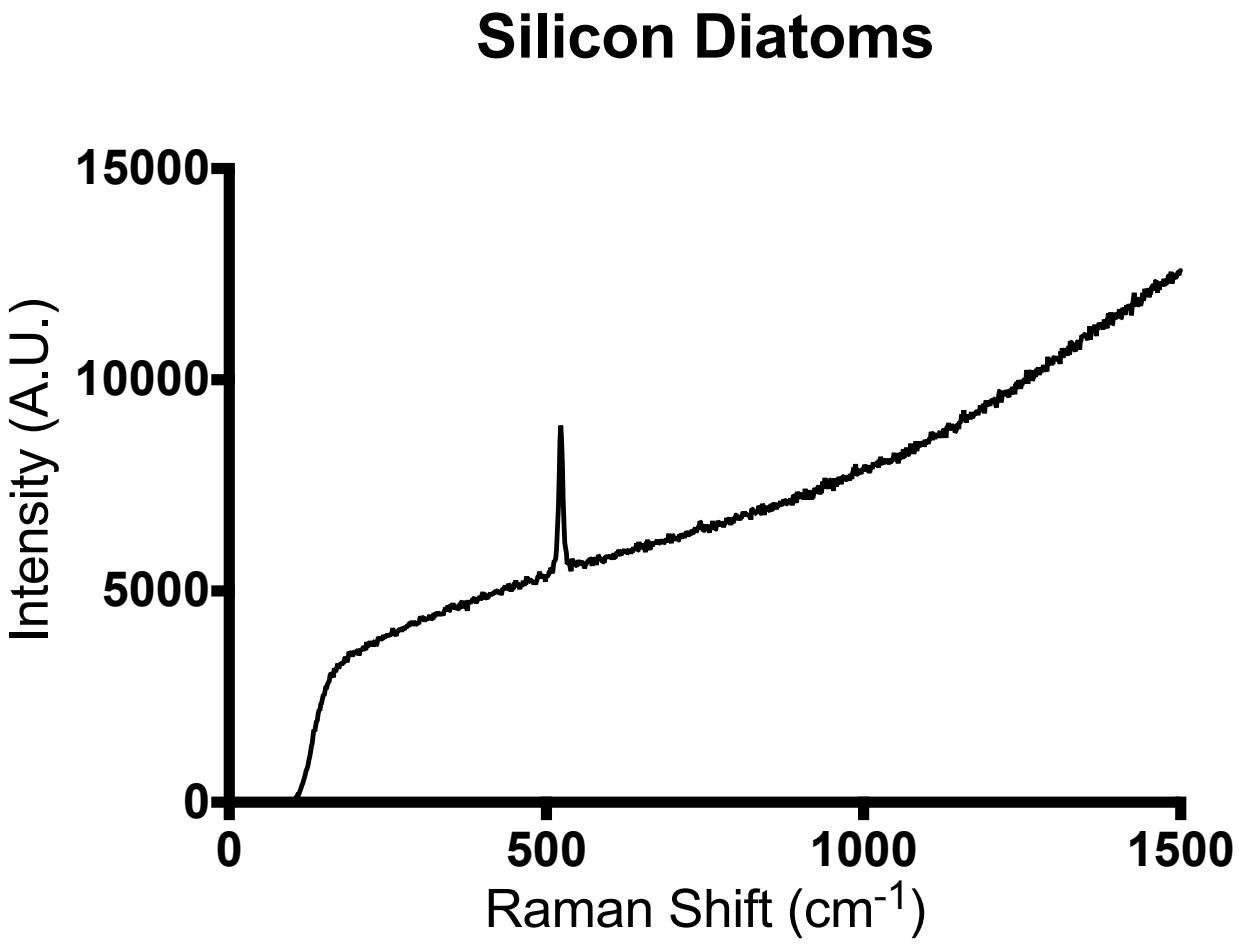

Figure 2: Silicon Raman showing an intensity increase at 521 cm^{-1}, a characteristic signature for crystalline silicon.

XRD was performed on the unreduced, HCl etched and heat-treated diatoms at ranges from 700°C – 850°C. The XRD showed that heat treatment at these temperatures transitioned the amorphous silica, the naturally occurring form found in the diatom frustule, to crystalline quartz as shown in Figure 3. The range of 20° to 80° 2θ was chosen because within this range the primary and secondary peaks can be seen clearly as well as the many minor peaks that all agree well with JCPDS card No. 46-1045.

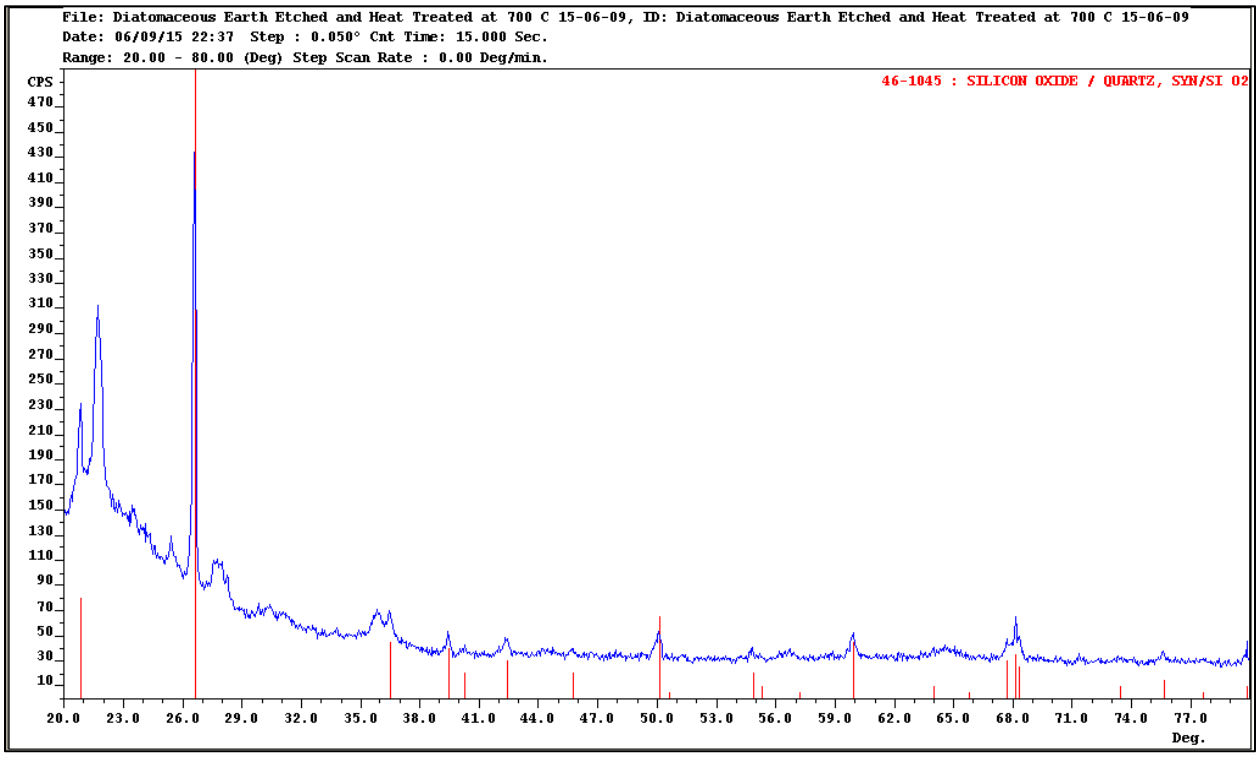

Figure 3: XRD of diatomaceous earth after performing the HCl etch heat treatment from 20 to 80 degrees 2θ.

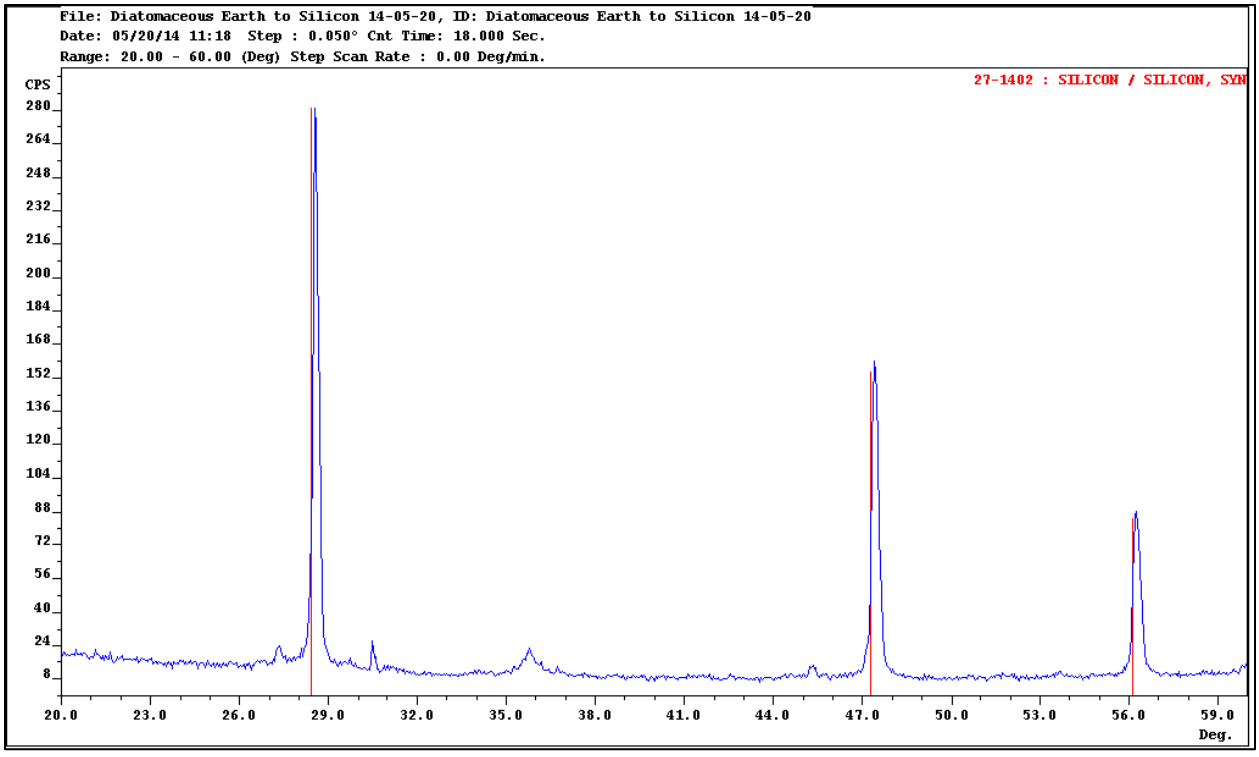

Figure 4: XRD of diatomaceous earth after performing a magnesiothermic reduction to convert it from amorphous silica to crystalline silicon from 20 to 60 degrees 2θ.

XRD was then performed on the magnesiothermicly reduced diatoms to confirm that crystalline silicon was the dominant crystal structure of the sample as shown in Figure 4. The XRD spectrum above shows the three majors peaks that are characteristic to silicon and correspond to JCPDS card No. 27-1402. The smaller peaks seen in the spectra are most likely due to the formation of magnesium silicate ($MgSi_2O_4$) as this byproduct is not removed by the post etching steps. The drift seen of 0.2 degrees to the right is most likely due to the sample holder not being at the optimal height for analysis.

The Scanning Electron Microscope (SEM) was used to look at the diatom frustules before coating them with a conductive carbon layer. Figure 5 and Figure 6 show images of the diatom frustules before and after magnesiothermic reduction, respectfully. Looking closely into the pores of the diatom frustule seen in Figure 5, the pores are intact, having an array of smaller pores in each of the individual larger pores of the frustule. A similar diatom frustule was found after magnesiothermic reduction of the diatoms shown in Figure 6. The diatom frustule shown here does not contain the intact smaller pores in the individual larger pores. This shows that this thin layer of silica was reduced and removed from the pores due to the magnesium reaction scavenging oxygen atoms from silica.

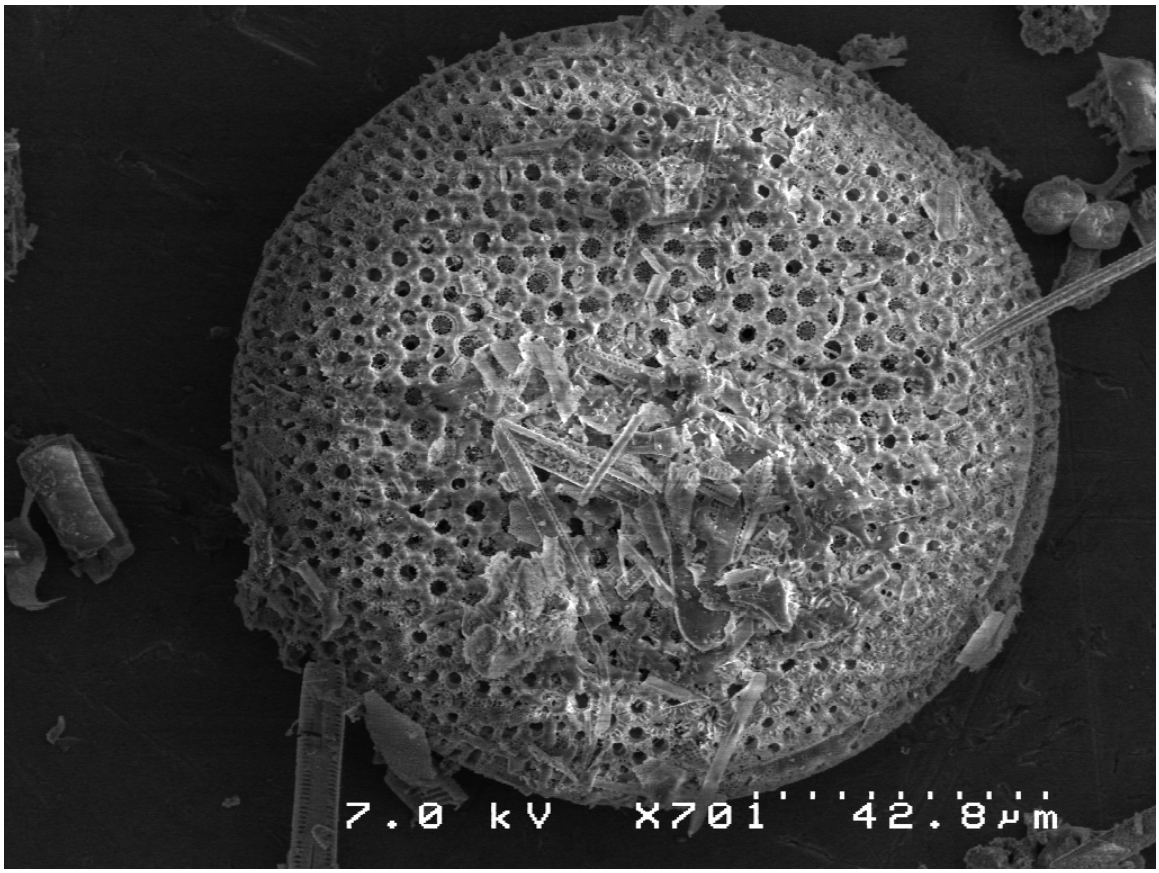

Figure 5: SEM image of the top surface of a diatom showing intact pores before magnesiothermic reduction process.

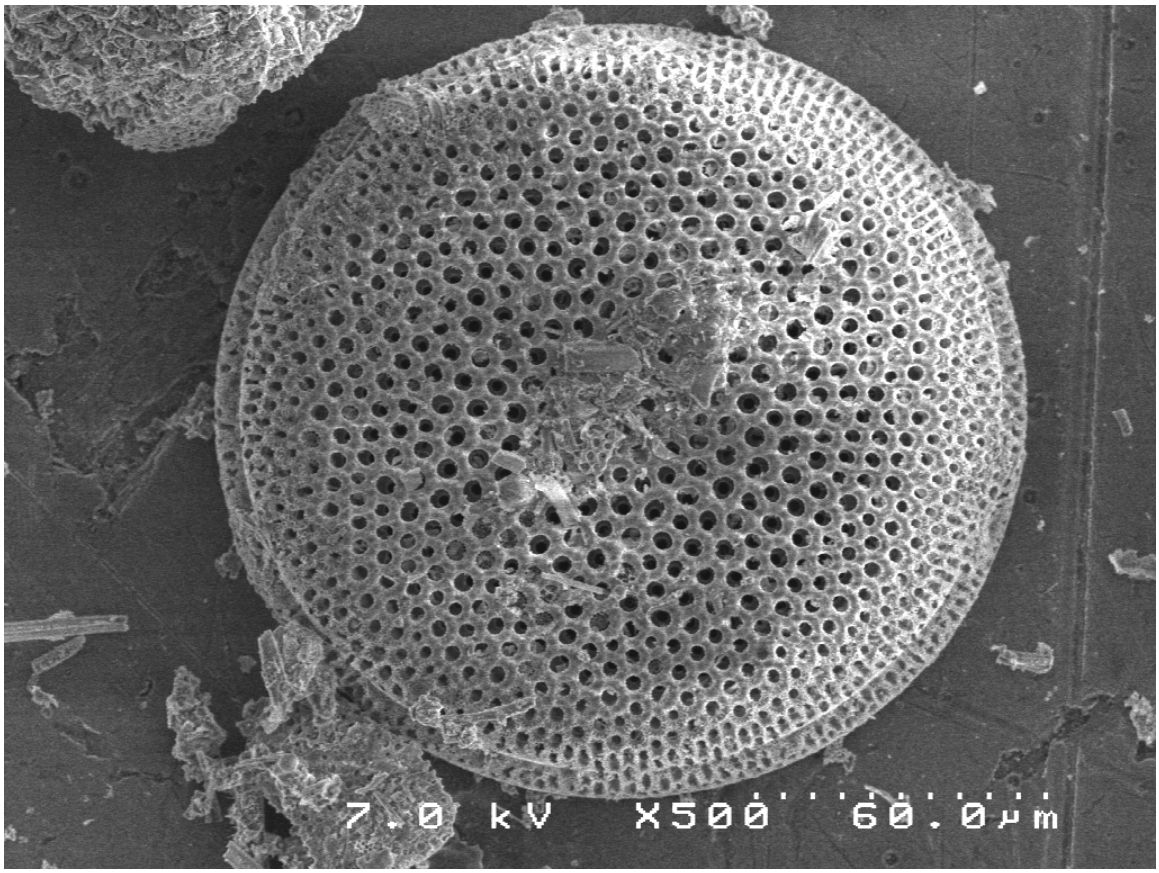

Figure 6: SEM image of the top surface of a similar diatom showing the pores removed after the magnesiothermic reduction process.

Transmission Electron Microscope (TEM) was used to view the carbon lattice formation on the frustule surface shown in Figure 7. This indicates that a graphene (graphite) layer was deposited onto the surface of the frustule a few nanometers thick. This graphene (graphite) coverage of the frustule allows for increased electron flow, as the silicon is a semiconductor by nature. This thin layer of carbon creates a nanocomposite structure in which the diatoms are homogeneously covered from the CVD process. The makes a ductile and active matrix to help with expansion and election conductivity. The carbon coating yields an active matrix that has a relatively low mass, good in terms of electronic conductivity, expresses small volume expansion, and has a reasonable Li-insertion capability.

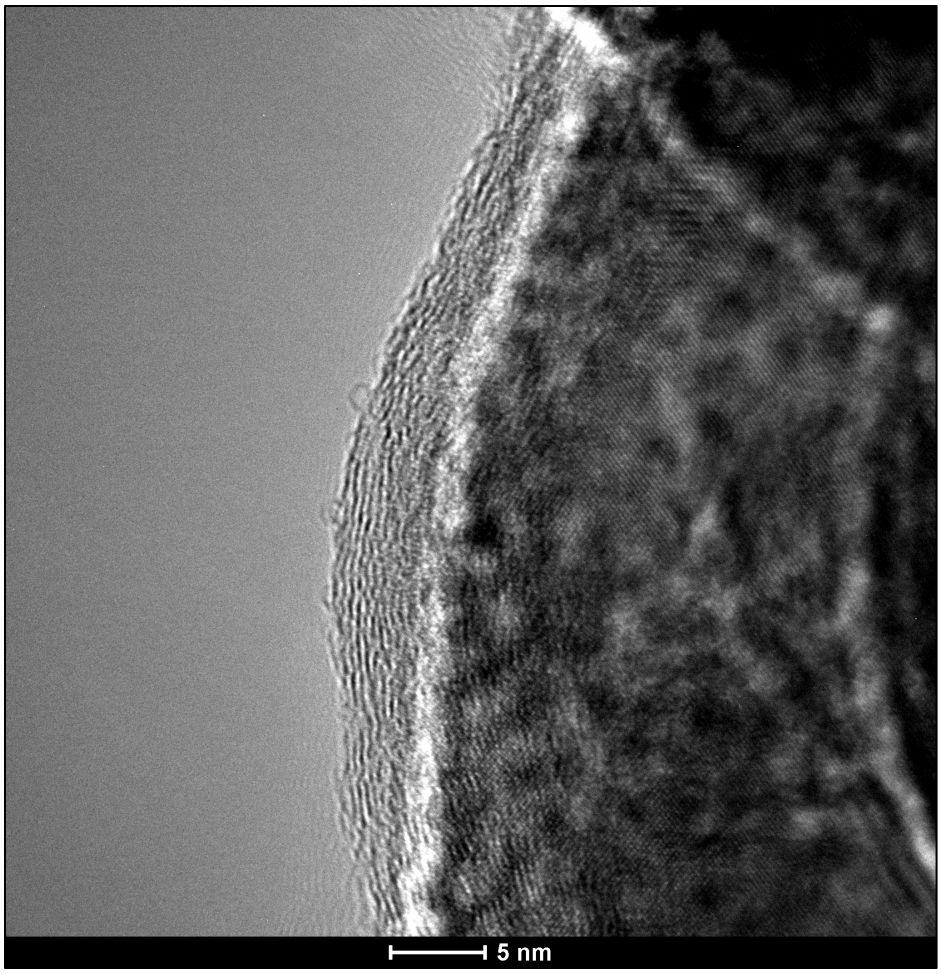

Figure 7: TEM of diatom frustule after carbon coating. The carbon lattice can be seen on the frustule surface indicating thin layer coverage a few nanometers thick.

Figure 7 shows a charge – discharge curve of the lithium-ion battery coin-cell using the carbon-coated silicon frustule as an anode and a lithium metal plate as the cathode and reference electrode. At a constant current density of 100 mA g^{-1} these coin-cell were galvanostatically charged and discharged between a voltage of 0.02 – 2.0 V. (The potential or voltage difference between the electrodes verses Li^{+}/Li). Only 3 cycles were ran to test the overall stability and capacity limit of the coin-cell.

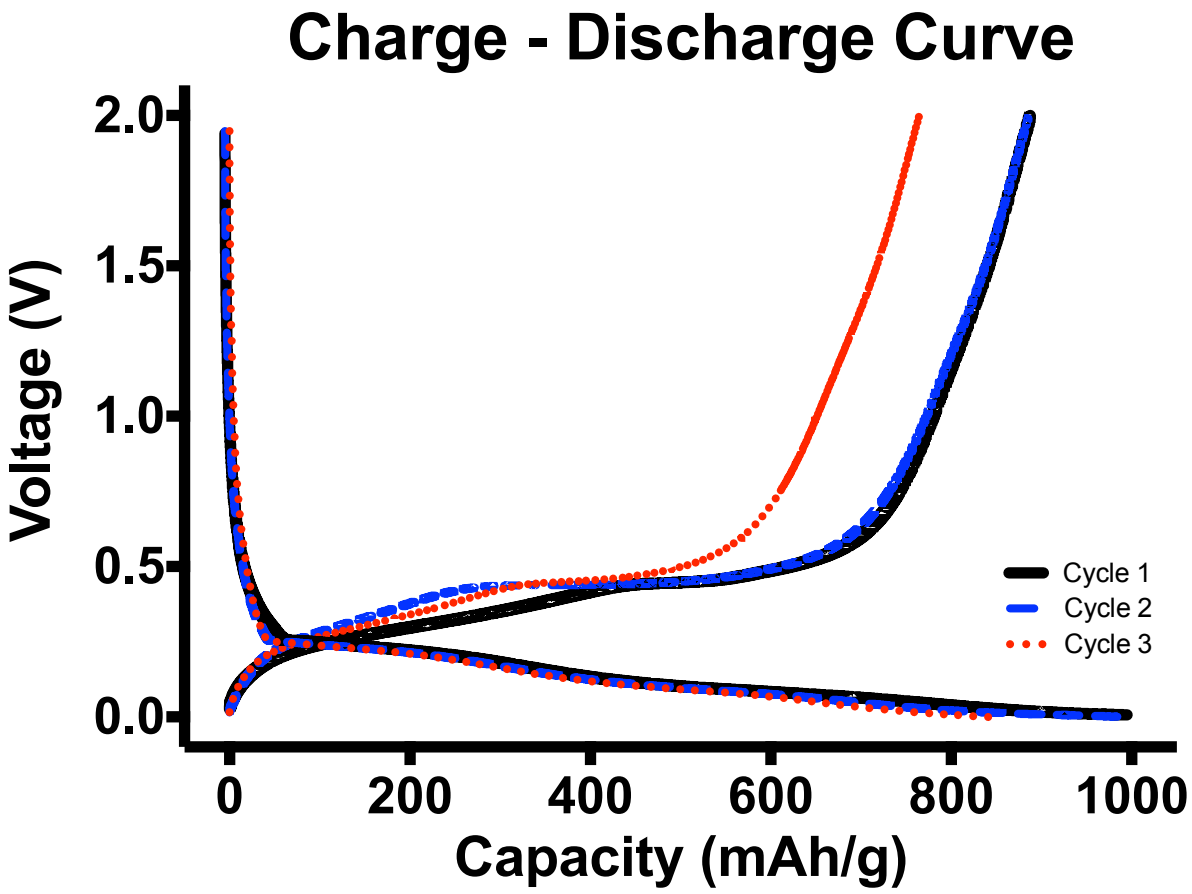

Figure 8: Charge – Discharge curve of an assembled battery using diatoms as the anode material. (Charge moving from left to right and Discharge moving from right to left.)

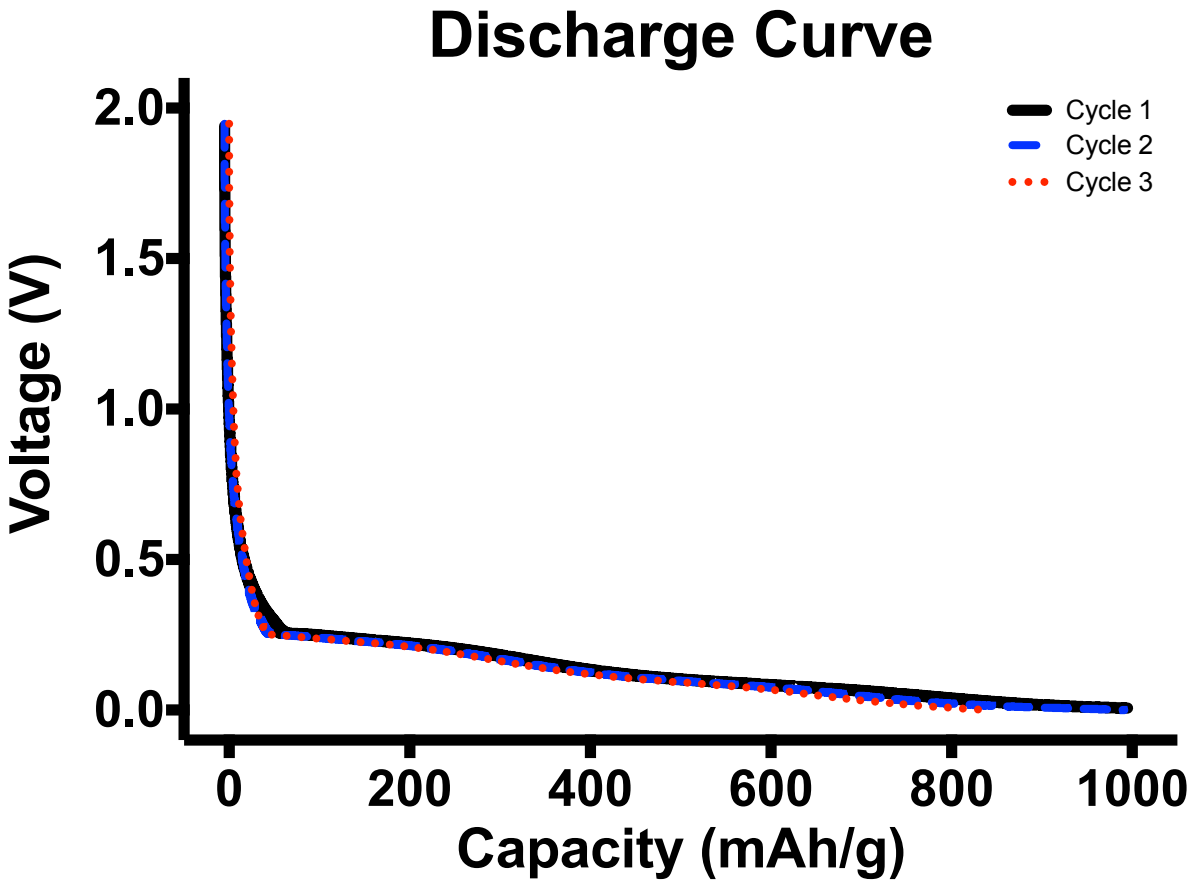

Figure 9: The discharge curve of the charge-discharge curve. Voltage is seen to drop quickly then slowly discharge to end-of-discharge.

Figure 9 shows the discharge curve were delithiation of the anode occurs *i.e.* the intercalated lithium-ions leave the carbon-coated silicon frustule anode and migrate through the electrolyte to the solid lithium metal cathode while their associated electrons are collected by the current collector and then recombine with the lithium-ions at the cathode. Through this process the anode and cathode electrodes undergo concurrent oxidation and reduction reactions, respectively. Starting at the 2.0 V mark, the discharge curve is seen to drop very rapidly and then the slope almost flattens, but maintains a slope with a slight negative decent until end-of-discharge. This sudden drop is due to the internal resistance of the system bringing the working potential window of silicon between 0.0 and 0.4 V for lithium-silicon alloying. The threshold for competitive commercial materials is 1000 mAh g^{-1}. Cycles 1 and 2 perform sufficiently well reaching the 1000 mAh g^{-1} mark. Cycle 3 shows a sharp decrease of approximately 150 mAh g^{-1} in capacity, dropping the overall total capacity to 850 mAh g^{-1}. The most likely cause for this loss in capacity is due to the structural deformity of the crystalline silicon after the second charge – discharge cycle.

As lithium intercalates into silicon, silicon's crystal lattice increases in volume by approximately 400%. Upon compression silicon to its normal crystal lattice state, the ability for breaks and pulverization can occur leading to discontinuities in the silicon lattice. This can cause lithium-ions to more slowly to intercalate into the silicon on the next cycle due to the electrons not being able to flow into the silicon continuously to the lithium-ion site for alloying because the electrons cannot jump gaps and need to find longer routes to these sites. If major breaks occur and islands of silicon are formed, then the electrons cannot combine with the lithium due to the discontinuity of the silicon lattice leading to less lithium incorporation, and overall less capacity of the battery.

Reading the graph from right to left starting near the 0.0 V mark, the charge curve can be read as shown in Figure 10. Following the slow, steady positively increasing slope to the plateau seen in the graph is indicative of the lithiation process in which the lithium-ions and electrons are leaving the solid lithium metal cathode and moving back to the carbon-coated silicon frustule anode.

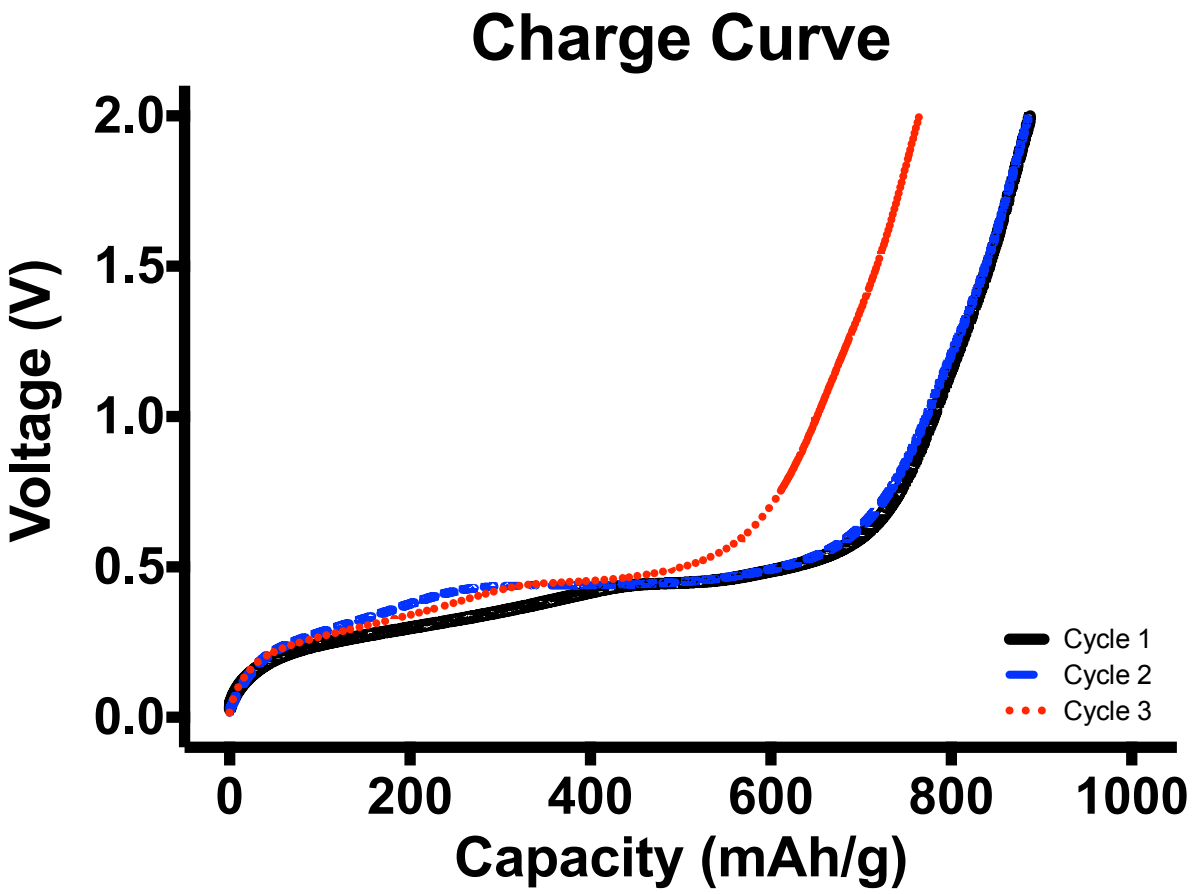

Figure 10: The charge curve of the charge-discharge curve. Voltage is seen to slowly increase at first, and then plateau before increasing with a quick upward trend.

The slower charge rate at 100 mA g^{-1} allows for the mass transfer and diffusion of the lithium-ions from the cathode through the bulk of the electrolyte and the eventual intercalation of the lithium-ions into the carbon-coated silicon frustule anode. This plateau shows the maximum rate of charge that this system can undergo before the termination voltage is reached. The sharp, upward curve seen in graph, starting at approximately 650 mAh g^{-1}, is when plating of the lithium-ions onto the anode starts to occur. As seen similarly in the discharge curve, the 1st and 2nd cycles of the charging cycle have relatively good agreement with each other reaching a capacity of approximately 887 mAh g^{-1}. The charge capacity diminishes to approximately 765 mAh g^{-1} for the 3rd cycle. This initial capacity decrease seen in the 1st and 2nd cycles as well as the capacity decrease seen in the 3rd cycle is most likely due to the lithium-ions plating to the carbon-coated silicon frustule anode. Lithium plating causes a reduction in the free lithium-ions available in the system, which leads to an irreversible reduction in the capacity. Plating can occur when the lithium-ions cannot intercalate into the silicon at a steady rate and the lithium-ions start to coat the surface of the anode. In addition to capacity loss of the system, lithium plating is not homogeneous across the anode surface, but more likely to form dendritic structures. These dendritic structures can span between the anode to the cathode and cause short-circuiting of the battery.

There are many reasons for the sub-optimal performance for this lithium-ion diatom battery system. Lithium plating and silicon crystal structure deformities are the biggest factors for the reduced performance in maintaining a high capacity. The deformities of the silicon crystal structure are the most likely cause of capacity loss for the lithium-ion battery system seen in the charge – discharge curves above. The large loss of capacity is seen after the second charge – discharge cycle, which points to the silicon breaking and pulverizing underneath itself trying to

reestablish its original crystal structure. These breaks would lead to trapped electrons and lithium-ions in silicon anode islands that are not in contact with the metal plate. Electrons would not be allowed to move through the current collector nor would the lithium-ions be allowed to move out of the anode and diffuse through the electrolyte and back to the cathode. This is seen in Figure 9 when the third cycle fails to release all the lithium-ions from the anode to the cathode and again in Figure 10 when the lithium-ions are not able to intercalate as deeply. In both cases, electrons are not able to meet the lithium-ions due to breaks in the silicon impeding the electrons from separating and recombining with the lithium-ions and further impeding the lithium-ions from alloying and dealloying with the silicon.

Future Directions

Further optimization is needed for the diatom-based anode battery to raise the overall capacity and to increase the cycling lifetime. Using a single species of diatom for purposes of constructing the diatom-based anode will allow for monodisperse uniform morphology, increased packing efficiency, and uniform volume expansion of porous silicon. Using the diatom species *Thalassiosira pseudonana* will allow for the monodisperse uniform morphology sought after for the anode because of the unique characteristic of the species. During division, the disparity of mother cell and daughter cell is very minimal allowing for the desired monodisperse cultures. Using the *Thalassiosira pseudonana* diatom species for lithium-ion battery anode development will allow for increased optimizations needed to better lithium-ion technology.

Chapter 3

SYNTHESIS AND CHARACTERIZATION OF DIATOMS TO ELEMENTAL SILICON

Introduction

Using diatomaceous earth has shown promise in Li-ion battery development without the need of a clean room to develop a working silicon anode. The data from the last chapter suggests that using diatomaceous earth is a feasible alternative to the all carbon anode that is currently being used commercially. While diatomaceous earth is easy to acquire, it contains a plethora of diverse diatom species of all morphologies, including broken and whole diatom frustules. It was speculated that with the large polydispersity of the frustules within the diatomaceous earth from one batch to the next might allow for discontinuities in electron flow. Due to the uncontrollable sizes and shapes given from the diatomaceous earth, growing a controllable, monodisperse culture of diatoms may allow for further optimization of this anode by using a single species of diatoms.

The diatom species, *Thalassiosira pseudonana* (*T. pseudonana*), is used in this project due to their monodisperse nature when growing cultures. Diatoms have a high surface area to volume ratio because they of their hierarchical micro- and nano-scale features. These structural features of the diatom's frustule are periodic, two–dimensional pore arrays. The unique porous arrays across the entire diatom are used for interaction with its external environment and for resource sequestration of nutrients and precursors for cell division. These porous array features contribute to the high surface area to volume ratio of the amorphous silica frustule. By using an organism that self-manufactures these porous arrays, which are usually are obtained by etching

silicon with hydrofluoric acid (but there is no control on the porosity or the porous design created), and using a species that is very consistent in regards to monodispersity, this provides a very unique and less complex alternative to established methods that use more complicated routes and toxic precursors.

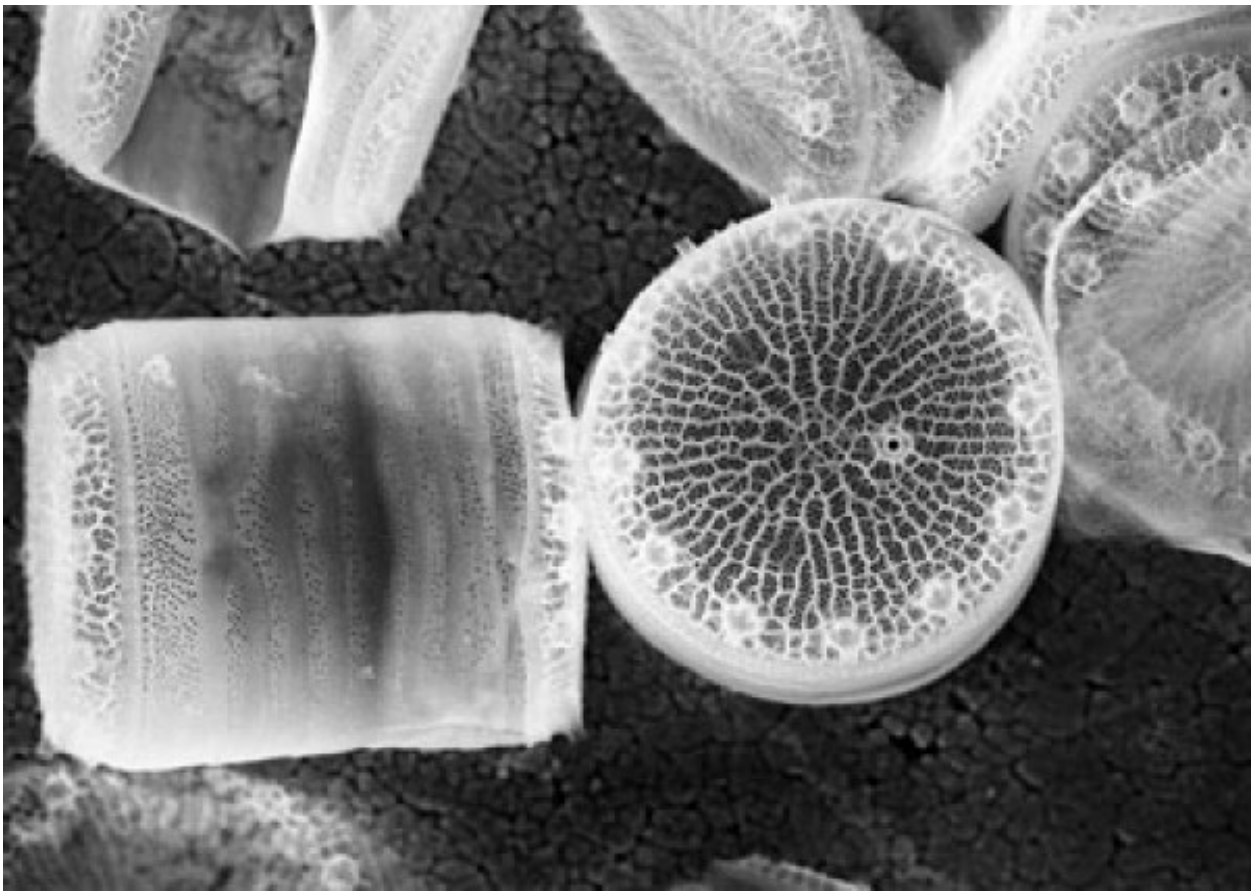

Figure 11: SEM image of *Thalassiosira pseudonana*, showing the side and top profiles of the diatom.[1]

The *T. pseudonana* as seen in Figure 11, is unique in comparison to other diatom species during its cell division step. The common cell division observed in diatoms exhibits the McDonald–Pfitzer principle, where a petri dish style division is seen and over time, the average size of the diatom reduces by the thickness of the top theca width.[34,35] This means that the mother cell maintains its original dimensions and the daughter cell's dimensions are reduced. The division occurs at the girdle band of the diatom, a region where supportive bands of silica hold the overlapping top and bottom sections, called thecae, of the frustule together. The thecae slide apart while simultaneous additions of new girdle band elements are acquired from the environment to form the inner, newer thecae. The thecae remain intimately linked throughout this process The *T. pseudonanas* are unique in this process because they have a very thin girdle band in comparison, making the mother and the daughter cells have almost no disparity in their dimensions. By using this unique characteristic, monodisperse cultures can be generated and harvested from for controlled morphologies in materials research.

Experimental Methods

Diatom Growth

Diatoms are grown in controlled conditions that most mimic their natural environment. This is achieved by growing the *T. pseudonana* in artificial seawater made by the Artificial Sea Water Medium (ASWM) recipe seen in Appendix B. In a temperature controlled room, the temperature is held constant at 63°F (~17.22°C). The light and dark cycle used for the diatoms was a 16:8 hour light/dark cycle controlled by a plug-in mechanical timer. Philips cool white fluorescent bulbs were used to aid the diatoms with photosynthesis and provide a higher amount of blue wavelengths for growth. The bulbs were rated at a Lux of 4035, within the range needed

for the photosynthetic processes of the diatoms. This high lux amount allows the light to penetrate the surface of the diatom culture and make sure that all the diatoms are photo-irradiated. The measured Lux, from the bulb distance to 1 cm deep from the surface layer of the diatom culture, was found to be approximately 3,620 Lux (in light 3,960 Lux). The overall distance from the bulb surface to the bottom surface of the diatom culture was 25 cm (22.5 cm from the top surface of the diatom culture). The bulb Lux was tested using a 3251 Traceable® Duel-Range Light Meter from VWR® to ensure the proper wavelengths were present for the diatoms.

Diatom Recovery and Preparation

Millipore® filters (0.2 μm diameter), were used extract the diatoms from the ASWM. The dimensions of the *T. pseudonana* are 4 – 5 μm in width and 4 – 6 μm in length. This makes the diatoms easily isolated from their media using these filters. The *T. pseudonana* frustules were cleaned by first soaking the frustules in 10% (v/v) hydrochloric acid (HCl) solution for 8 hours at 80°C to remove any metal impurities in or associated to the frustule by forming metal-chlorides. The Millipore® filters also dissolve in this HCl solution and temperature condition. This allows the diatoms to be removed from the filter for recovery later. After cleaning with 10% HCl, the solution was allowed to cool to room temperature and the frustules were recovered by aspiration using the same Millipore® filters initially. The frustules were washed with copious amounts of water and a final wash of ethanol was used. The cleaned frustules were then transferred onto a quartz combustion boat and spread evenly across the bottom surface for maximum surface area coverage to make sure all the material was exposed evenly in the tube furnace. The boat was then placed into a tube furnace and set to 90°C at a ramp rate of 2.5°C per minute and held for 10 minutes, then ramped to 700ºC for 30 minutes to remove any organic material from the frustule

and to remove the dissolved filters based on Thermal Gravimetric Analysis (TGA) performed previously Appendix C.

Results and Discussion

XRD of the *T. pseudonana* diatom frustules was taken after the preparation step. Figure 12 shows the XRD of the unreduced, HCl etched, heat-treated *T. pseudonana* diatom frustules. The XRD spectrum shows good agreement with the JCPDS card No. 46-1045 within the range of 20° to 80° 2θ having the primary, secondary, many of the minor peaks showing good alignment. A slight drift of 0.2º 2θ can be seen in the spectrum due to the small amount of material recovered from the preparation step of the diatom frustules. The heat-treatment of the diatom frustules seems to be moving the amorphous silica structure normally found in *T. pseudonana* frustules to a more order quartz crystalline structure.

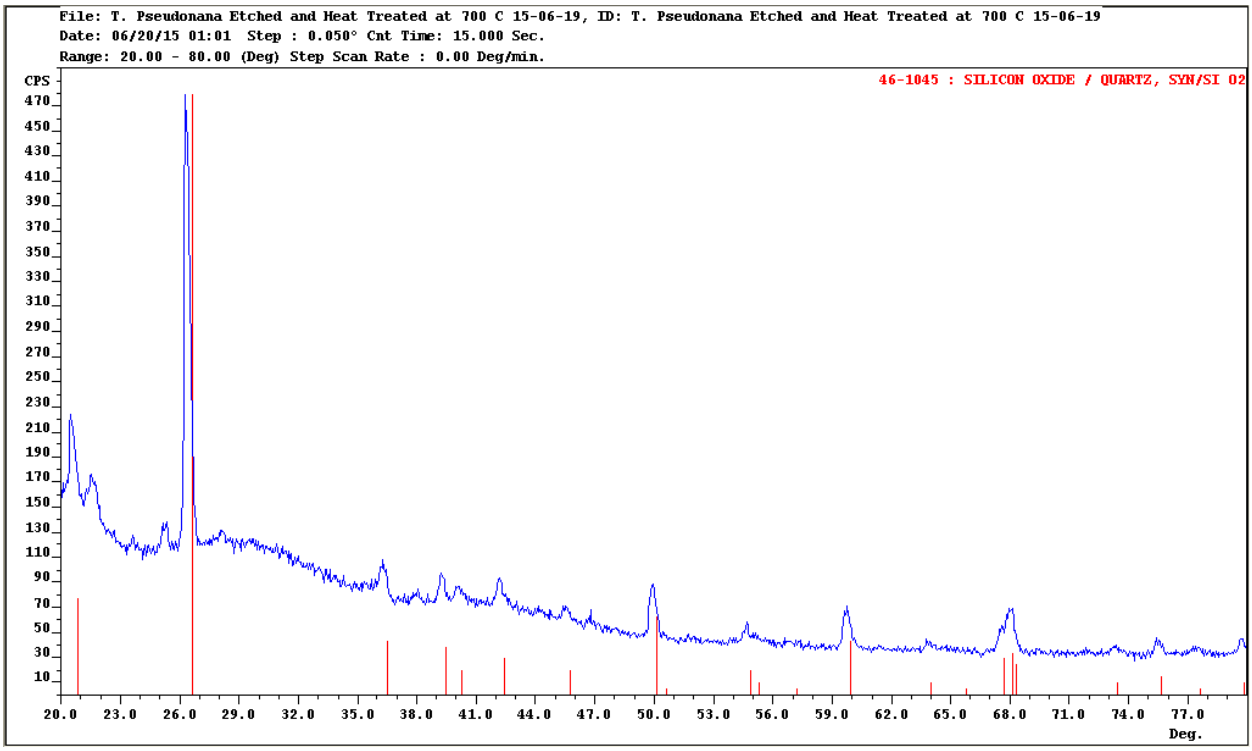

Figure 12: XRD of *T. pseudonana* frustules after performing the HCl etch heat treatment from 20 to 80 degrees 2θ.

Future Directions

The diatom, *T. pseudonana*, shows promise good silicon precursor and as a battery anode based on the results from the past chapter and the preliminary results found in this chapter. Due to many difficulties with culturing large quantities of the *T. pseudonana* diatom species as well as loss of equipment, this section of the project was unable to be completed.

Other directions that the diatom structure could more toward could be filtration systems or sensing. The porous array on the diatom and its overall structure makes it ideal for small sediment and small molecule filtration when a graphene coat is applied for non-specific interactions with fat and protein molecules, viruses, microbes, funguses, toxins, waste by-products, wastewater, salts and as well as a plethora of other water soluble and insoluble impurities unwanted for drinking water.

This thesis has provided only one of the many uses of diatoms and their unique frustule structure. There are many other directions and applications that the diatom frustules can be utilized in and using their hierarchical structure as a platform to further materials research is just a fraction of their potential.

APPENDIX A

Equation For Pressure Inside the MTRC

$$PV = nRT$$

$$P = \frac{\frac{m}{M}RT}{V}$$

$$T = 500°C = 773.15K$$
$$V = 19mL = 0.019L$$
$$R = 0.08205746_{14}\frac{L \bullet atm}{K \bullet mol}$$
$$n = \frac{m}{M}$$

$$0.13g + 0.18g = 0.31g \bullet 4 = 1.24g$$
$$0.52g + 0.72g = 1.24g$$

$$\frac{0.52\text{g}}{28.0855\,{}^{g}\!/_{mol} + 2 \bullet 15.9994\,{}^{g}\!/_{mol} \bullet 2} + \frac{0.72g}{24.3050\,{}^{g}\!/_{mol}} = 0.03828mol$$

$$P = \frac{\left(\frac{0.52\text{g}}{28.0855\,{}^{g}\!/_{mol} + 2 \bullet 15.9994\,{}^{g}\!/_{mol} \bullet 2} + \frac{0.72g}{24.3050\,{}^{g}\!/_{mol}}\right) \bullet 0.08205746_{14}\frac{L \bullet atm}{K \bullet mol} \bullet 773.15K}{0.019L} = 127.82atm$$

APPENDIX B

Artificial Sea Water Medium[36,37]

Solid Chemicals (g)	1 Liter	1.5 Liter	2 Liter	3 Liter	4 Liter	6 Liter	8 Liter
NaCl	23.6	35.4	47.2	70.8	94.4	141.6	188.8
$CaCl_2 \cdot 2H_2O$	1.1	1.65	2.2	3.3	4.4	6.6	8.8
Gylclyglycine	0.67	1	1.34	2	2.68	4	5.36

Liquid Stocks (mL)							
Solution I	33.3	50	66.7	100	133	200	267
Solution II	16.7	25	33	50	66.7	100	133
Trace Elements	1	1.5	2	3	4	6	8
$Na_2SiO_3 \cdot 9H_2O$ (10% solution)	1.2	1.8	2.4	3.6	4.8	7.2	9.6

Adjust pH to 8.0 a 10% NaOH solution

After autoclaving add (mL)							
0.1 M K_2HPO_4, (Autoclaved separately)	2	3	4	6	8	12	16
Vitamin Stock	1	1.5	2	3	4	6	8

Vitamin Stock

200 mg Thiamine-HCl
4 mg Vitamin B12
2 mg Biotin
*Dissolve in 1 liter H_2O, filter sterilized. Store at 4ºC.

Liquid Stocks

	1 liter	2 liter
Solution I		294 g $MgSO_4 \cdot 7H_2O$ 246 g $MgCl_2 \cdot 7H_2O$
Solution II	0.137 g H_3BO_3 0.72 g $Na_2EDTA \cdot 2H_2O$ 45 g KCl 18 g KNO_3	

***Make Solution I and II in polycarbonate bottles**

Trace Elements

	Per liter
H_3BO_3	0.586 g
$ZnCl_2$	0.624 g
$CuCl_2 \cdot 2H_2O$	0.268 g
$NaMoO_4 \cdot 2H_2O$	0.252 g
$CoCl_2 \cdot 6H_2O$	0.42 g
$FeSO_4 \cdot 7H_2O$	2.49 g
$NaC_4H_4O_6 \cdot 2H_2O$ (Na tartrate)	1.77 g
$MnCl_4 \cdot 4H_2O$	0.36 g
Na_2SeO_3 (sodium selenite)	Make 1000 x stock (0.173 g/liter and add 1 mL per liter of T. elements stock

APPENDIX C

TGA of *T. pseudonana* and Millipore® filters

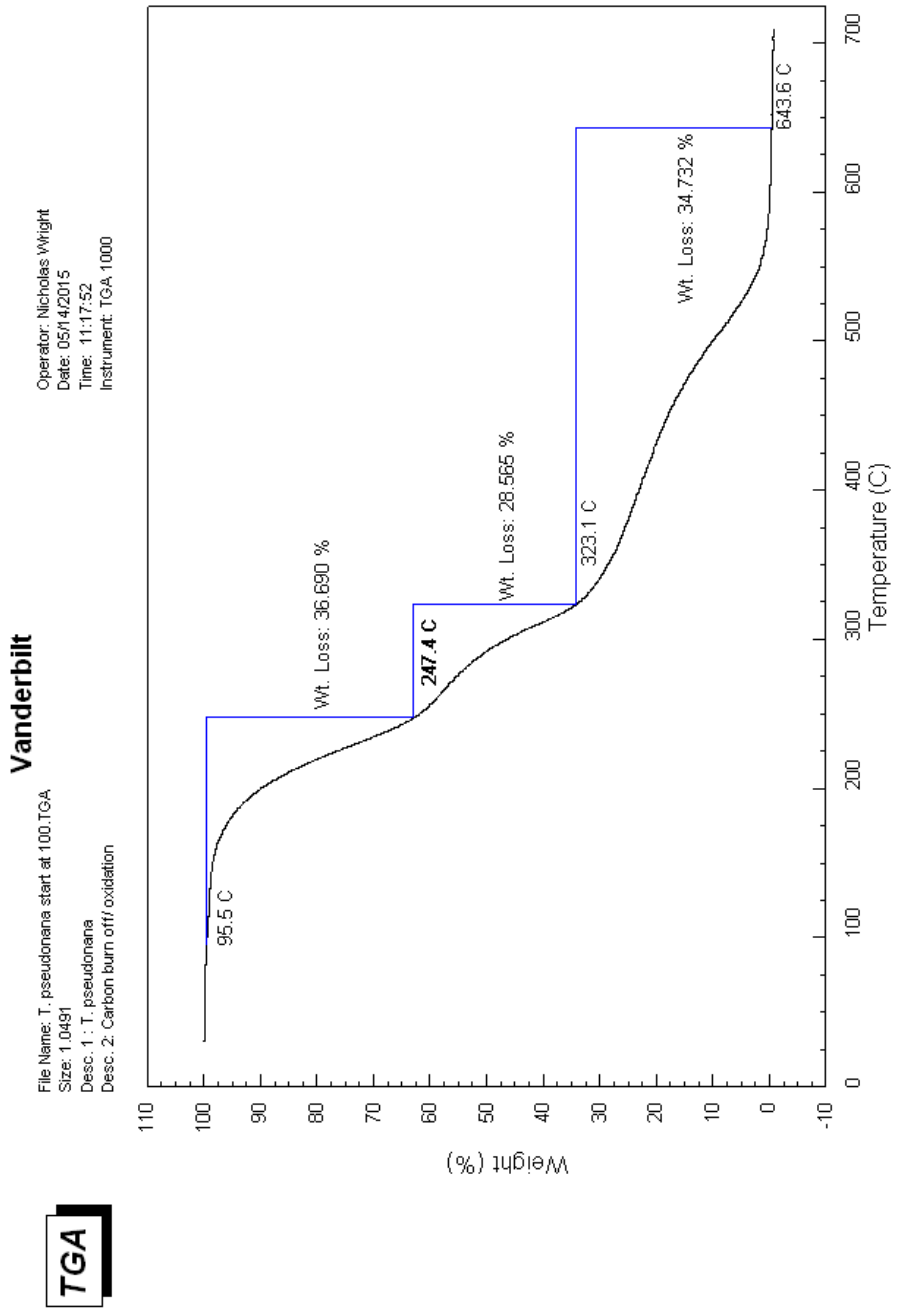

Figure 13: TGA of *T. pseudonana* and Millipore® filters showing oxidation of organic material leaving ~0.14 mg of diatom frustules.

REFERENCES

(1) Pennisi, E. In *Science News*; Science: Web, 2004; Vol. Biology.

(2) Buchmann, I.; Inc, C. E. *Batteries in a Portable World: A Handbook on Rechargeable Batteries for Non-engineers*; Cadex Electronics, 2001.

(3) Round, F. E.; Crawford, R. M.; Mann, D. G. *The Diatoms: Biology & Morphology of the Genera*; Cambridge University Press, 1990.

(4) Mann, S. *Biomineralization: principles and concepts in bioinorganic materials chemistry*; Oxford University Press, 2001; Vol. 5.

(5) Simpson, T. L.; Volcani, B. E. *Silicon and siliceous structures in biological systems*; Springer-Verlag, 1981.

(6) Martin-Jézéquel, V.; Hildebrand, M.; Brzezinski, M. A. *Journal of Phycology* **2000**, *36*, 821.

(7) Crawford, S. A.; Higgins, M. J.; Mulvaney, P.; Wetherbee, R. *Journal of Phycology* **2001**, *37*, 543.

(8) Richter, O. *Zur physiologie der Diatomeen*; Aus der Kaiserlich-Königlichen Hof- und Staatsdruckerei, in Kommission bei A. Hölder, 1906; Vol. 2.

(9) Lewin, J. C. *Plant Physiology* **1955**, *30*, 129.

(10) Azam, F.; Hemmingsen, B.; Volcani, B. *Arch. Microbiol.* **1974**, *97*, 103.

(11) Paasche, E. *Limnology and Oceanography* **1980**, *25*, 474.

(12) Hildebrand, M.; Volcani, B. E.; Gassmann, W.; Schroeder, J. I. *Nature* **1997**, *385*, 688.

(13) Drum, R. W.; Pankratz, H. S. *American Journal of Botany* **1964**, *51*, 405.

(14) Kröger, N.; Deutzmann, R.; Sumper, M. *Science* **1999**, *286*, 1129.

(15) Kröger, N.; Lorenz, S.; Brunner, E.; Sumper, M. *Science* **2002**, *298*, 584.

(16) Sumper, M. *Science* **2002**, *295*, 2430.

(17) Luckarift, H. R.; Spain, J. C.; Naik, R. R.; Stone, M. O. *Nat Biotech* **2004**, *22*, 211.

(18) Knecht, M. R.; Wright, D. W. *Langmuir* **2004**, *20*, 4728.

(19) Lenoci, L.; Camp, P. J. *Langmuir* **2008**, *24*, 217.

(20) Schmid, A. *Mikroskopie* **1976**, *32*, 81.

(21) Schmid, A.-M. M.; Schulz, D. *Protoplasma* **1979**, *100*, 267.

(22) De Stefano, L.; Rendina, I.; De Stefano, M.; Bismuto, A.; Maddalena, P. *Applied Physics Letters* **2005**, *87*, 233902.

(23) Wu, H.; Yu, G.; Pan, L.; Liu, N.; McDowell, M. T.; Bao, Z.; Cui, Y. *Nat Commun* **2013**, *4*.

(24) Cho, J. *Journal of Materials Chemistry* **2010**, *20*, 4009.

(25) Chan, C. K.; Peng, H.; Liu, G.; McIlwrath, K.; Zhang, X. F.; Huggins, R. A.; Cui, Y. *Nat Nano* **2008**, *3*, 31.

(26) Holmes, J. D.; Johnston, K. P.; Doty, R. C.; Korgel, B. A. *Science* **2000**, *287*, 1471.

(27) Kim, H.; Seo, M.; Park, M.-H.; Cho, J. *Angewandte Chemie International Edition* **2010**, *49*, 2146.

(28) Smol, J. P.; Eugene F. Stoermer, e. *The Diatoms*; Cambridge University Press, 2010.

(29) Oakes, L.; Westover, A.; Mares, J. W.; Chatterjee, S.; Erwin, W. R.; Bardhan, R.; Weiss, S. M.; Pint, C. L. *Sci. Rep.* **2013**, *3*.

(30) Drees, L. R.; Wilding, L. P.; Smeck, N. E.; Senkayi, A. *Minerals in soil environments* **1989**, *2*, 913.

(31) Walther, J. V.; Helgeson, H. C. *Am. J. Sci* **1977**, *277*, 1315.

(32) Keskar, N. R.; Chelikowsky, J. R. *Physical Review B* **1992**, *46*, 1.

(33) Srikar, V. T.; Swan, A. K.; Unlu, M. S.; Goldberg, B. B.; Spearing, S. M. *Microelectromechanical Systems, Journal of* **2003**, *12*, 779.

(34) Pfitzer, E. H. H. *Untersuchungen über Bau und Entwicklung der Bacillariaceen (Diatomaceen)*; Marcus, 1871.

(35) Piganeau, G. *Genomic Insights Into the Biology of Algae*; Academic Press, 2012.

(36) Darley, W. M.; Volcani, B. E. *Experimental Cell Research* **1969**, *58*, 334.

(37) Darley, W. M.; Volcani, B. *Methods in enzymology* **1971**, *23*, 85.